

Journal of Biomedical Optics

BiomedicalOptics.SPIEDigitalLibrary.org

Morphological phenotyping of mouse hearts using optical coherence tomography

Michelle Cua
Eric Lin
Ling Lee
Xiaoye Sheng
Kevin S. K. Wong
Glen F. Tibbits
Mirza Faisal Beg
Marinko V. Sarunic

Morphological phenotyping of mouse hearts using optical coherence tomography

Michelle Cua,^{a,*} Eric Lin,^b Ling Lee,^{b,c} Xiaoye Sheng,^c Kevin S. K. Wong,^a Glen F. Tibbits,^{b,c} Mirza Faisal Beg,^a and Marinko V. Sarunic^{a,*}

^aSimon Fraser University, Faculty of Applied Science, School of Engineering Science, 8888 University Drive, Burnaby, BC V5A 1S6, Canada

^bSimon Fraser University, Faculty Science, Department of Biomedical Physiology and Kinesiology, 8888 University Drive, Burnaby, BC V5A 1S6, Canada

^cChild and Family Research Institute, Department of Cardiovascular Science, 950 West 28th Avenue, Vancouver, BC V5Z 4H4, Canada

Abstract. Transgenic mouse models have been instrumental in the elucidation of the molecular mechanisms behind many genetically based cardiovascular diseases such as Marfan syndrome (MFS). However, the characterization of their cardiac morphology has been hampered by the small size of the mouse heart. In this report, we adapted optical coherence tomography (OCT) for imaging fixed adult mouse hearts, and applied tools from computational anatomy to perform morphometric analyses. The hearts were first optically cleared and imaged from multiple perspectives. The acquired volumes were then corrected for refractive distortions, and registered and stitched together to form a single, high-resolution OCT volume of the whole heart. From this volume, various structures such as the valves and myofibril bundles were visualized. The volumetric nature of our dataset also allowed parameters such as wall thickness, ventricular wall masses, and luminal volumes to be extracted. Finally, we applied the entire acquisition and processing pipeline in a preliminary study comparing the cardiac morphology of wild-type mice and a transgenic mouse model of MFS. © The Authors. Published by SPIE under a Creative Commons Attribution 3.0 Unported License. Distribution or reproduction of this work in whole or in part requires full attribution of the original publication, including its DOI. [DOI: 10.1117/1.JBO.19.11.116007]

Keywords: optical coherence tomography; cardiac imaging; morphometric analysis; computational anatomy.

Paper 140470R received Jul. 21, 2014; revised manuscript received Sep. 24, 2014; accepted for publication Sep. 26, 2014; published online Nov. 13, 2014.

1 Introduction

Transgenic mouse models have proven to be invaluable in research to understand the etiology behind a wide variety of cardiovascular pathophysiology. The changes in cardiac morphology and functioning in response to targeted gene manipulations can provide insight into the origin and progression of cardiovascular dysfunction. For example, mouse models have been beneficial in elucidating the etiology behind Marfan syndrome (MFS), a multisystemic genetic connective tissue disorder that affects approximately 1 in every 5000 to 10,000 individuals.^{1,2} MFS can result from numerous different genetic mutations normally in the fibrillin-1 (*FBNI*) gene, and has a short untreated life expectancy mainly due to its cardiovascular complications, such as aortic dilation and dissection. Using histology, researchers have been able to study the changes in aortic wall composition, structure, and size in transgenic mouse models of MFS. These histological studies provided valuable insight that linked specific fibrillin-1 mutations and the severity of the disease.³⁻⁶

Mouse models have also been beneficial in elucidating the mechanisms behind other cardiovascular diseases, such as myocardial infarction and congenital heart disease.^{7,8} Although histology has been successfully used to study some pathological changes in the heart, other structural anomalies have been difficult to visualize as the sectioning plane limits the field-of-view. In these cases, a global, three-dimensional (3-D) image of the

heart would be useful for locating structural anomalies and determining the optimal sectioning plane. 3-D visualization is also valuable as it allows researchers to study the heart macroscopically, which can yield important information about morphological abnormalities due to disease. Techniques such as episcopic fluorescence image capture allow for the acquisition of 3-D cross-sectional volumetric information at a cellular resolution, but, as with conventional histology, require destructive tissue sectioning.⁹

Other techniques, such as echocardiography, cardiac magnetic resonance (CMR) imaging, and microcomputed tomography (μ CT), provide 3-D datasets without microsectioning and are important *in vivo* medical imaging techniques. Echocardiography is the preferred imaging modality for *in vivo* functional imaging due to its high temporal resolution. Commercially available ultrahigh-frequency ultrasound systems (20 to 100 MHz) offer higher spatial resolution, up to tens of microns, which is sufficient to resolve many important physiological parameters, such as ventricular wall thickness and ejection fraction. However, due to the tradeoff in depth of penetration and probe frequency, most *in vivo* adult mouse applications are centered on using 40 to 50-MHz probes, which offer spatial resolutions on the order of 50 μ m.¹⁰ Moreover, since echocardiography cannot propagate through bone or air, images of the heart can only be acquired through specific unobstructed windows, which limit its scope. Compared to echocardiography, CMR and μ CT are not hampered by imaging depth or resolution. Instead, their use in *ex vivo* applications is limited by a high imaging cost in the case of CMR, and a low soft-tissue contrast in the case of μ CT. Although contrast-enhancement dyes can be used for μ CT,

*Address all correspondence to: Michelle Cua, E-mail: emc2@sfu.ca; Marinko V. Sarunic, E-mail: msarunic@sfu.ca

detailed visualizations of smaller features, such as cardiac valves, chordae tendinae, or smaller vasculature are still hard to obtain.⁹

Thus, there is a need for a cost-effective imaging modality that can image the whole mouse heart with high spatial resolution. One potential modality is optical coherence tomography (OCT). Similar to echocardiography, OCT utilizes the back-reflected signal to generate depth-resolved, cross-sectional images and does not specifically require the use of tissue sectioning or exogenous contrast agents. In comparison to echocardiography, OCT provides 3-D volumetric datasets with higher spatial resolution and intrinsic tissue contrast, making it easier to visualize structures such as the coronary vasculature and the myocardial fiber bundles. Moreover, the 3-D nature of the acquired OCT datasets allows researchers to better locate and quantify both the local and global morphological changes in the heart, as, unlike histology, OCT does not require any tissue sectioning. In fact, since OCT is nondestructive, traditional histological approaches, such as immunohistochemistry, can be used as a complementary, follow-up approach to further investigate the tissue structure and composition at a higher resolution.

In this report, we describe the imaging and 3-D image processing steps necessary to use OCT as a cardiac imaging modality, and then validate the approach by comparing the cardiac morphologies of wild-type (WT) mice against a transgenic mouse model of MFS. Although OCT offers micrometer-scale resolution, it has a limited penetration depth, ~1 to 2 mm in cardiac tissue,^{11,12} making it difficult to resolve internal structures such as the valves or inner surface of the walls of a mouse heart.

We present a novel, multifaceted approach involving optical clearing and multiperspective imaging to increase the penetration depth of OCT without sacrificing resolution. After acquisition, the volumes were corrected for refractive distortion to facilitate the creation of a single, volumetric reconstruction of the whole mouse heart. Finally, we describe the image processing pipeline necessary to make quantitative comparisons of the cardiac morphology between multiple hearts, and present preliminary findings studying the differences in cardiac morphology between WT mice and a transgenic mouse model of MFS.

2 Methods

2.1 Animal Preparation

All experimental protocols were performed at the Child and Family Research Institute (CFRI) with approval from the Animal Ethics Board of the University of British Columbia and are in accordance with the Canadian Council on Animal Care Regulations. Three WT ($Fbn1^{+/+}$) and five MFS ($Fbn1^{C1039G/+}$) mice were used in this study. All mice were 12 months of age. The founder Marfan mouse models were graciously provided by Dr. HC Dietz at Johns Hopkins University and were bred in the CFRI animal care facility.

In preparation for extracting the heart, the mice were first anesthetized by 2% to 3% isoflurane with oxygen and then heparinized (100 μ L, at 1000 U/mL and 5000 U/kg) via an intraperitoneal injection. After the disappearance of the toe pinch response, the hearts were excised via a midsternal thoracotomy. The aorta was cannulated and retrogradely perfused using a Langendorff apparatus with Tyrode's solution (4 min at 2 mL/min) and 4% paraformaldehyde (30 min at 2 mL/min) to remove the blood and fix the tissue. The fixed heart was stored

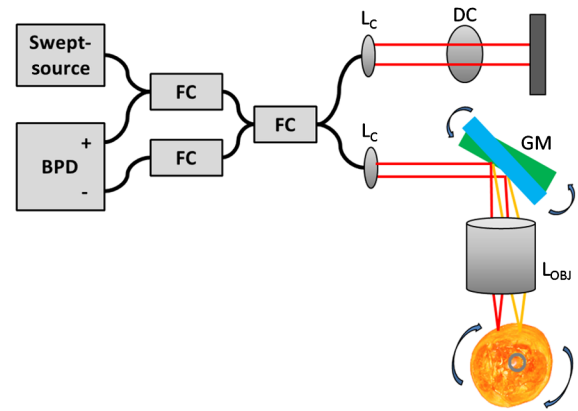


Fig. 1 Schematic of the high-resolution 1060-nm swept-source optical coherence tomography system used to image the mouse hearts. The hearts were rotated about the long axis as shown. FC, wavelength-flattened fiber couplers; DC, dispersion compensation block; BDP, balanced photodiode detector; GM, galvanometer-scanning mirrors; L_C , collimating lens; L_{OBJ} , telecentric objective lens.

at 4°C in phosphate-buffered saline. Prior to imaging, the hearts were cleared via immersion in glycerol using a graded protocol (50% and 70% for 1 day each).

2.2 Data Acquisition

A custom-built 1060-nm swept-source optical coherence tomography (SS-OCT) system was used to image the hearts (Fig. 1). For the light source, we used a commercial swept-source engine (Axsun Technologies, Massachusetts) that had an effective 3-dB bandwidth of 85 nm, resulting in a calculated axial resolution of 7 μ m in air. Light was focused on the sample using a telecentric scan lens (LSM04-BB, Thorlabs, New Jersey) that had an effective focal length of 54 mm, thereby yielding a transverse resolution (full-width-half-maximum) of 15 μ m in air.

Due to the limited depth of penetration and imaging depth of our OCT system, the whole adult mouse heart could not be imaged from a single perspective. Instead, multiple volumes were acquired at 30-deg increments, rotating the heart about its long axis across the entire 360-deg span. At each rotation, 10 volumes were acquired and averaged to further offset the loss in signal-to-noise from the telecentric scan lens and glycerol clearing. Data acquisition was performed using an open-sourced program that utilized graphics processing units (GPUs) to allow for real-time visualization of the dataset.¹³ Each volume consisted of $1408 \times 400 \times 800$ voxels, with each voxel having a physical dimension of $2.6 \times 21.1 \times 18.0 \mu\text{m}^3$.

2.3 Removal of Image Distortions

The volumetric images of the mouse heart acquired from multiple perspectives were combined into a single volume of the whole heart. For the remainder of this paper, the volumes taken from different perspectives will be referred to as “subvolumes,” whereas the volume of the whole heart will be referred to as the “whole volume.” Prior to registering and stitching the subvolumes into a whole volume, distortions within the OCT volume due to the imaging process were corrected. In OCT, image distortions arising from nonlinear scanning distortion, nontelecentric scanning distortion, and refraction cause registration mismatch and decrease the accuracy of the quantitative measurements.^{14–16} We minimized the scan-related distortions

by employing a telecentric lens as our objective lens and by considering only the linear portion of the scan in our data acquisition.

The refractive distortions arising from the epicardial surface of the heart were minimized in postprocessing. To correct for refraction, the refractive indices of each layer as well as the boundaries between the layers were determined. Since the heart was immersed in 70% glycerol prior to imaging, and glycerol permeates the tissue through passive diffusion, glycerol was assumed to be within the heart chambers as well. Given that the majority of the refraction occurs at the air-to-tissue interface, the algorithm only corrected for distortion due to refraction at the epicardial surface of the heart.

The outermost surface of the heart was automatically segmented in 3-D using a gradient-based approach. The volumes were first despeckled using 3-D edge-preserving bounded-variation (BV) smoothing.¹⁷ After denoising, the volumes were then convolved with 3-D Sobel filters to obtain three gradient volumes, G_x , G_y , and G_z . The gradient magnitude, G , was then calculated for each voxel using $G = \sqrt{G_x^2 + G_y^2 + G_z^2}$ and then masked such that only the gradient within the tissue was nonzero [Fig. 2(b)]. The volumetric mask was computed by first applying morphological opening and closing on the BV-smoothed volume to remove other image artifacts, such as spots from bright back-reflections, and then automatically thresholding the volume [Fig. 2(c)]. After masking, the topmost nonmasked gradient point in each A-scan was labeled as a point belonging to the outermost surface [Fig. 2(d)].

For each slow-axis scan, the segmented surface was adjusted to ignore wrapping due to complex-conjugate artifact. The wrapped portion of the image was detected by taking into account the convex nature of the ventricular surface. The inflection point was detected in the segmented surface through the second derivative test. For the part of the image past the inflection point, the bottom surface was segmented and unwrapped, and the actual surface of the heart was estimated using interpolation. Using this method, the segmentation algorithm was able to ignore wrapping due to complex conjugate artifact and detect the outermost surface of the heart [Fig. 2(e)].

After determining the co-ordinates of the top surface, we then corrected for refractive distortions using a similar approach to previously published and validated results.^{15,16} The refraction correction was based on the vector form for Snell's law, given by

$$\vec{V}_2 = \frac{n_1}{n_2} \vec{V}_1 - \left\{ \frac{n_1}{n_2} \vec{V}_1 \cdot \vec{N} - \sqrt{1 - \left(\frac{n_1}{n_2} \right)^2 [1 - (\vec{V}_1 \cdot \vec{N})^2]} \right\} \vec{N}, \quad (1)$$

where n_i is the refractive index of the i 'th material, \vec{V}_1 and \vec{V}_2 are the incident and refracted rays, and \vec{N} is the surface normal.^{15,18} Since we used a telecentric lens for the objective lens, we assumed that $\vec{V}_1(x, y, z) = \langle 0, 0, 1 \rangle$, where z denotes depth, and x, y denote the lateral position of each A-scan. The surface normal, \vec{N} , was computed by taking the cross product of the horizontal and vertical surface gradients. The length of

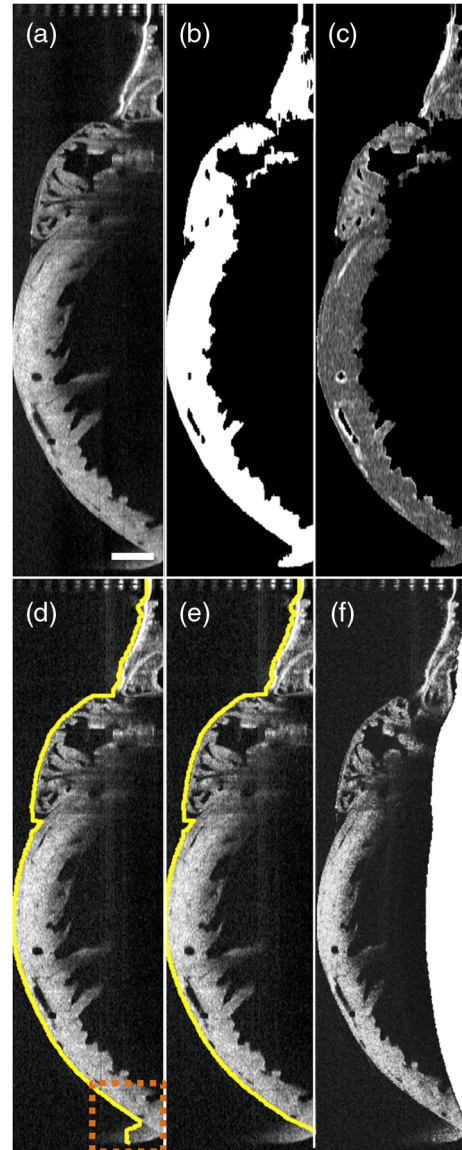


Fig. 2 Refraction-correction process shown on a representative slow-axis scan. (a) Original image. Scale bar denotes 1 mm. (b) Masked image computed to mask out noise in the gradient image. (c) Gradient image. (d) Image with segmented epicardial surface (solid yellow line). The orange box (dashed) denotes portion of the segmentation that was corrected to account for complex-conjugate artifact. (e) Adjusted segmentation result (solid yellow line). (f) Refraction-corrected image.

the refracted ray (optical path length) was also scaled by the refractive index.

Once the refracted ray was calculated, the image was then de-warped. For a given A-scan, the position of each voxel, $P(x, y, z)$, is given by

$$P(x, y, z) = \begin{cases} \vec{V}_2(x, y, z) & \text{if } \vec{V}_1(x, y, z) > S(x, y, z) \\ \vec{V}_1(x, y, z) & \text{otherwise} \end{cases}, \quad (2)$$

where S is the location of the segmented top surface, and P is the adjusted co-ordinate of the voxel. After calculating P , we interpolated the scattered data to find the one-to-one mapping between the refraction-corrected and original volume, and

applied 3-D bicubic interpolation to generate the refraction-corrected volume [Fig. 2(f)].

2.4 Volumetric Registration and Stitching

The refraction-corrected subvolumes were registered together to form a whole volume. 3-D rigid registration, with 6 degrees-of-freedom, was chosen to avoid introducing nonphysical distortions from nonrigid algorithms. Registration was performed using Amira (FEI, France), a commercial 3-D imaging analysis and processing software. To register multiple subvolumes together, we registered each volume to multiple template volumes. The volumes acquired from 90-deg perspectives (at 0 deg, 90 deg, 180 deg, and 270 deg) were first pairwise registered to form the skeleton of the cardiac geometry. The remaining volumes were then registered to their two closest neighbors; for example, the volume acquired at 30 deg was registered to the volumes acquired at 0 deg and 90 deg. In this manner, the registration errors were divided across the whole volume.

After registration, the subvolumes were stitched together to form a whole heart volume. Although the refraction correction procedure minimizes geometric distortion, small mismatches in the registered volumes due to residual distortions and registration errors remain. These small mismatches would result in a blurring of high frequency information if the volumes were stitched using simple averaging. To prevent the decrease in resolution associated with averaging, we implemented a 3-D version of multiband blending, whereby lower frequency information was averaged over a wider area, whereas high frequency information was averaged over a narrower region.^{19,20} The contribution of each volume was determined by calculating a priority function. For a set of $i = 1 \dots N$ subvolumes, a priority function P^i was calculated, where data with higher fidelity were given higher weight. The priority function was calculated using

$$P^i = \frac{1}{\sqrt{(x - x_c)^2 + (y - y_c)^2}}, \quad (3)$$

where x, y are the lateral scan positions, and x_c and y_c are the centers of the lateral scans. The stitching was performed in an iterative fashion, with one volume added to the final, stitched result per iteration. For more details as to how the priorities were used to blend the volumes together, please refer to the algorithm published by Brown and Lowe.²⁰

Figure 3 shows the contribution of each subvolume to the final, whole volume for a single, representative short-axis slice. Figure 3(c) shows the result of stitching the first two volumes, with the contribution of each volume shown using overlaid color. Figure 3(d) shows the final stitched result, with the contribution from each volume shown in Fig. 3(e). Although each slice is a composite from multiple subvolumes, registration and stitching artifacts are not easily distinguishable within the final result. The stitched result had a voxel size of $20 \times 20 \times 20 \mu\text{m}^3$.

2.5 Morphometric Analysis

Prior to performing the morphometric analysis, the atrioventricular valves and ventricular chambers and lumen were first segmented in each of the whole heart volumes. Figure 4 shows the steps of the semiautomatic segmentation process on two representative slices, a short-axis slice and a slice that shows the four chambers of the heart. Using Amira, the volume was first automatically thresholded using a hysteresis-based region-growing

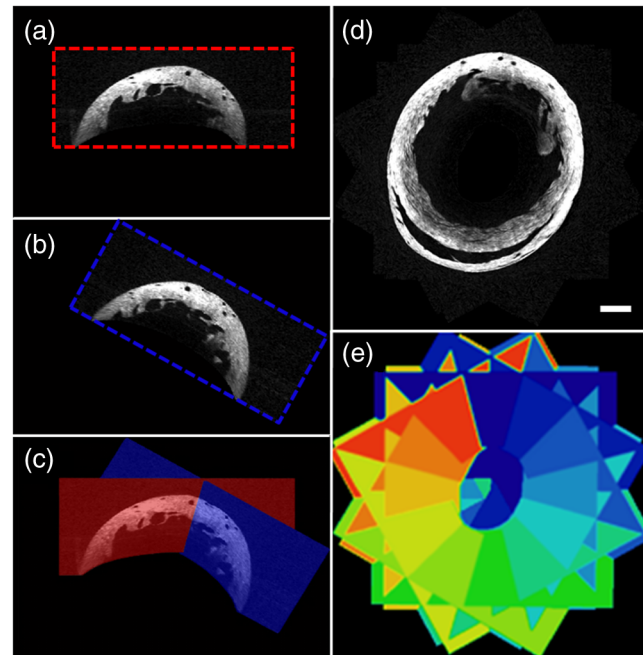


Fig. 3 Stitching of mouse heart subvolumes using multiband blending to maximize image resolution in the whole heart volume, as shown on a representative short-axis slice. (a)–(c) The stitching procedure on two subvolumes, with the first subvolume in (a), and the second in (b). The stitched result for the first two subvolumes is shown in (c), with the contributions from each overlaid in color. (d) The final short-axis slice stitched from all 12 subvolumes. (e) Contributions from the subvolumes to the final short-axis slice. The scale bar in (c) denotes 1 mm for the stitched result in (c) and (d).

algorithm. Although most of the cardiac tissue was automatically segmented, deeper regions that had greater signal attenuation were not always detected and required manual refinement [Fig. 4(b)]. Next, the atrioventricular valves, ventricular walls, and ventricular lumens were manually labeled in Amira [Fig. 4(c)], and the ventricular masses were calculated by considering the voxel dimensions, the number of voxels assigned to the ventricular wall, and the specific gravity of myocardium (1.055 g/cm^3). The luminal volumes were quantified in a similar manner.

After segmentation, the inner and outer boundaries of the ventricular walls were delineated. The trabeculae, which are muscular protrusions located on the endocardial surface of the heart, were removed using morphological closing to compute the thickness of the myocardium. After removing the trabeculae, the center of the left ventricle (LV) was estimated using a center-of-mass algorithm, and the image was unwrapped from that point. The boundaries of the right and left ventricles were then detected in the unwrapped image and converted back to Cartesian co-ordinates. The detected surfaces were spline-fitted to smooth the surface and resample it evenly. Spline fitting was performed by fitting the arc length of the detected surface to a spline function. Figure 4(d) shows the result of delineating the inner and outer surfaces of the right and left ventricular walls. The wall thickness at each point was then determined by defining the thickness to be the distance from the outer to inner wall in a direction perpendicular to the outer wall.

2.6 Realignment

The hearts were aligned to a standard orientation in order to facilitate comparison of similar regions across the sample set.

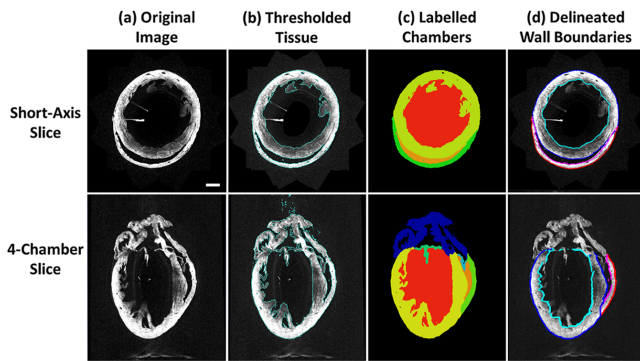


Fig. 4 Process of segmenting the heart chambers, shown on a representative short axis slice and four-chamber slice, in preparation for quantitative morphological analysis. (a) Original image. (b) Segmentation results after automatic thresholding using Amira, followed by manual refinement to remove noise and include low-intensity tissue regions. (c) Result after manually labeling the ventricular walls and lumen. (d) Image showing the detected inner and outer surfaces of the left and right ventricles. Labels for colored regions: yellow, left ventricular wall; red, left ventricular lumen; light green, right ventricular wall; orange, right ventricular lumen; light blue, left atrio-ventricular valve; dark blue, unlabeled structure. For segmented boundaries: dark blue, outer surface of LV wall; light blue, inner surface of LV wall; red, outer surface of RV wall; magenta, inner surface of RV wall. The scale bar on the upper left image denotes 1 mm.

Following conventions in the field of cardiac imaging, we aligned the vertical axis to the long axis of the left ventricle. The long-axis was estimated by modeling the left ventricle as an ellipsoid.^{21–23} The circumferential orientation was standardized by finding the mean direction of the right ventricle relative to the left ventricle.

3 Results

Figure 5 presents a representative four-chamber slice from an OCT dataset of the whole heart. Structures within the heart such as the interventricular septum and the atrioventricular valves can be visually identified. Details within the myocardial wall, such as coronary vasculature (blue inset) and myofibril bundles

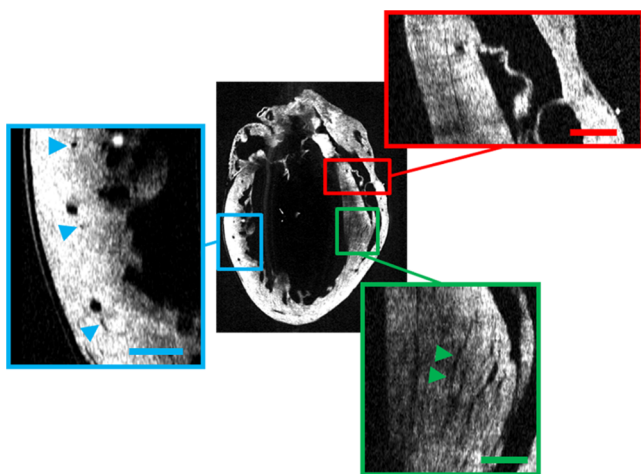


Fig. 5 Representative four-chamber slice from volumetric OCT dataset. The high resolution and tissue contrast of OCT permits visualization of smaller structures such as the valve leaflets (red inset, upper right), smaller coronary vessels (blue inset, left), and fiber bundles within the interventricular septum (green inset, lower right). Scale bars denote 500 μm . (Video 1, MOV 1.49 MB) [URI: <http://dx.doi.org/10.1117/1.JBO.19.11.116007.1>].

(green inset), are also visible. Video 1 provides a fly-through movie of a representative whole heart volume. To quantify the registration error, we analyzed the root mean square error (RMSE) between the physical rotation applied during image acquisition, and the rotation that was found using the registration process. The mean RMSE for the four hearts was $0.72 \text{ deg} \pm 0.12 \text{ deg}$. Since the rotation mount we used to rotate the cannula had a tolerance of 1 deg, our registered rotation agreed with the actual rotation.

3.1 Effect of Glycerol Concentration of Depth of Penetration

Figure 6 demonstrates the efficacy of glycerol clearing on increasing depth of penetration. At 0% glycerol, the endocardial surface of the left ventricle was not visible in the OCT B-scan. With the addition of glycerol, the OCT light source was able to penetrate the left ventricle completely, and details within the endocardial surface became apparent in the acquired image. Increasing the glycerol concentration increased the visible depth in the OCT imaging, but also decreased the contrast of the smaller features. We chose to use 70% glycerol as a compromise between the depth of penetration and the contrast.

3.2 Effect of Refraction Correction

The effect of refraction correction on the similarity of the contributions from the individual volumes is shown in Fig. 7, where three of the registered volumes have been placed in different RGB color channels. Refraction correction minimizes the artifactual differences in tissue thickness, and increases the coincidence of tissue structures across the individual volumes [Figs. 7(c) and 7(d)].

3.3 Morphological Comparison of Multiple Hearts

To demonstrate the potential of using OCT in studying differences in cardiovascular morphology, we imaged and compared the hearts of three WT and five Marfan mice. Table 1 presents the physical characteristic of the mice, reported as mean \pm SEM. The body weights, ventricular volumes, masses, and ventricular mass-to-volume ratio were compared using a paired t-test, with significance set at $p < 0.05$. The luminal volumes and masses were normalized by body weight. Comparing the WT and Marfan mouse model, the MFS mice exhibit significantly smaller mass-to-volume ratios (1.00 ± 0.01 versus $1.24 \pm 0.06 \text{ mg}/\mu\text{L}$) and larger normalized LV volumes

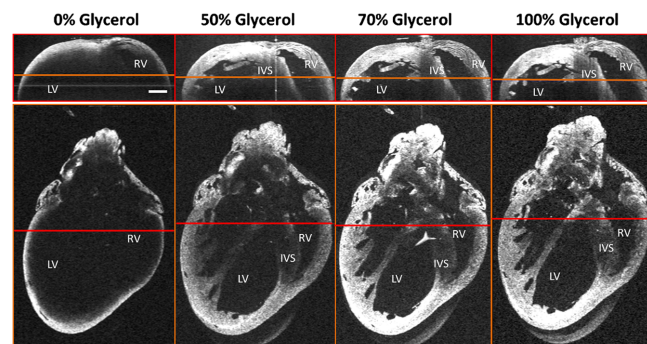


Fig. 6 Effect of glycerol on depth of penetration shown for clearing with 0%, 50%, 70%, and 100% glycerol concentrations. The scale bar on the upper left image denotes 1 mm.

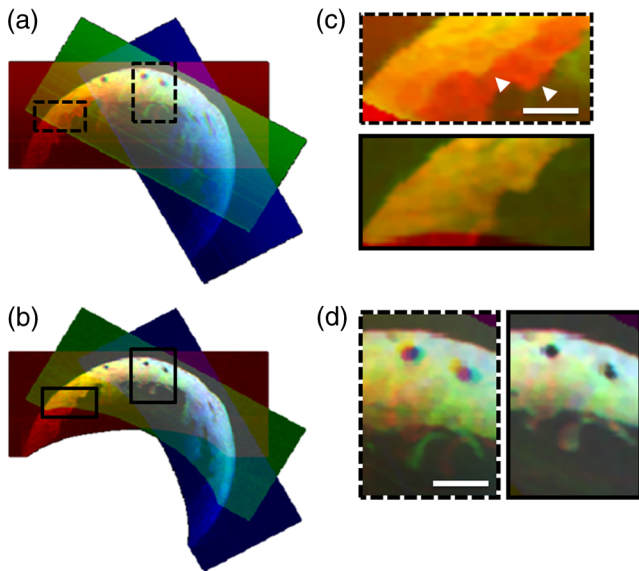


Fig. 7 Improvement in registration match with refraction correction. The result of registration is shown using the contributions from the first three registered volumes on a representative short-axis slice, with each volume occupying a different channel in the RGB image. (a) Result of registration with noncorrected volumes. (b) Result of registration with refraction-corrected volumes. Insets (c) and (d) highlight the difference in thickness, and location of structures without refraction correction, respectively. The locations of the insets are shown in (a) and (b), with the noncorrected results in dashed borders, and the corrected results in solid border. The scale bars in insets (c) and (d) denote 500 μm .

Table 1 Comparison of body weight, and ventricular mass and luminal volumes between the Marfan ($n = 5$) and wild-type ($n = 3$) mice.

	Marfan	Wild-type	p
BW (g)	36.78 ± 1.79	43.63 ± 2.17	0.054
RV volume (μL)	14.97 ± 2.53	10.27 ± 2.45	0.264
RV volume/ BW ($\mu\text{L/g}$)	0.42 ± 0.09	0.24 ± 0.05	0.195
RV mass (mg)	33.93 ± 2.53	34.68 ± 2.42	0.85
RV mass/BW(mg/g)	0.92 ± 0.05	0.80 ± 0.06	0.173
RV mass/volume (mg/ μL)	2.51 ± 0.40	3.68 ± 0.67	0.156
LV volume (μL)	110.56 ± 8.92	97.29 ± 7.47	0.35
LV volume/BW ($\mu\text{L/g}$)	3.01 ± 0.21	2.24 ± 0.18	0.047*
LV mass (mg)	110.69 ± 9.17	120.59 ± 11.45	0.529
LV mass/BW (mg/g)	3.01 ± 0.21	2.76 ± 0.19	0.451
LV mass/volume (mg/ μL)	1.00 ± 0.01	1.24 ± 0.06	0.002**
RV/LV volume	0.14 ± 0.03	0.10 ± 0.02	0.387

All values are reported as mean \pm SEM. * indicates $p < 0.05$, while ** indicates $p < 0.005$.

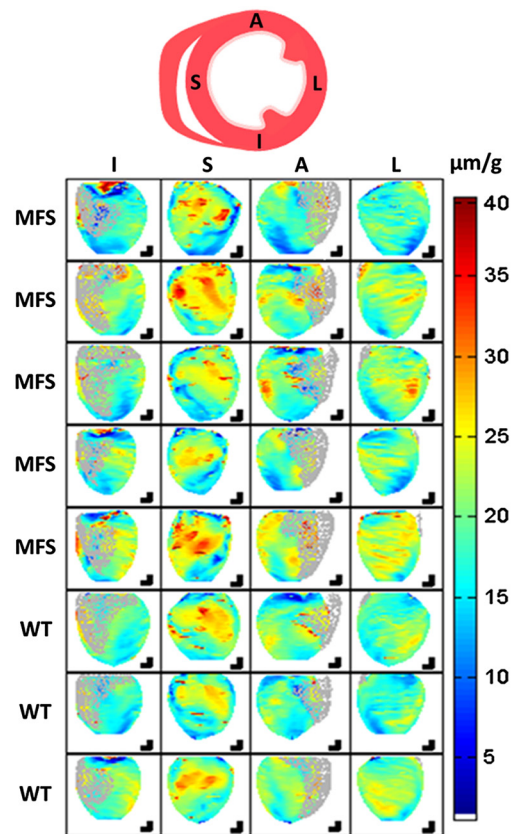


Fig. 8 Comparison of normalized left ventricular wall thickness between Marfan and wild-type mice, with thickness shown as a heat map. Topmost diagram shows relative location of the anterior (A), inferior (I), septal (S), and lateral (L) portions of the LV wall. Gray points in the inferior and anterior views show relative location of the RV. Scale bars denote 1 mm. A, anterior; I, inferior; L, lateral; S, septal; MFS, Marfan syndrome; WT, wild-type.

($3.01 \pm 0.21 \mu\text{L/g}$ versus $2.24 \pm 0.18 \mu\text{L/g}$), in MFS versus WT, respectively.

The thickness of the LV was computed across the entire wall and normalized by body weight to minimize the potentially conflicting effect of heart size.²⁴ Figure 8 compares the normalized wall thickness between the Marfan and WT mice. The thickness at a particular point has been displayed as a heat map, where blue represents the thinnest portions and red represents the thickest portions. The right ventricle has been shown in gray for the inferior and anterior views for orientation purposes. For display purposes, the LV wall was divided into four myocardial segments: anterior, lateral, septal, and inferior, as shown in Fig. 8. Comparing the WT and Marfan mice, the MFS mice exhibit slightly thicker walls relative to their WT counterparts.

4 Discussion

In this report, we demonstrated the feasibility of using OCT for phenotyping adult mouse hearts. Although OCT has been proven to be useful in characterizing the structure and function of embryonic hearts, the same demonstration has not been made yet in imaging the whole adult heart.^{9,25,26} Due to the limited depth of penetration (~ 1 to 2 mm in cardiac tissue) and trade-off between the depth of focus and spatial resolution, conventional OCT is unable to image the entire adult mouse heart

with high resolution. We bypassed the depth limitation by implementing multiperspective imaging and optical clearing. These subvolumes were then refraction-corrected to remove distortions that were introduced by the image acquisition process. We demonstrated the impact of refraction correction on minimizing registration mismatches between the subvolumes.

We also performed the first study comparing the cardiac morphology of WT and Marfan mice using OCT. We only quantified the global morphological changes since the focus of this project was in the development of OCT as a tool for cardiovascular phenotyping, and because other existing modalities, such as echocardiography and histology, are already able to evaluate changes in other parameters that are also relevant to MFS, such as the aortic root dimensions. Our results indicated that the Marfan mice exhibit significantly decreased left ventricular mass-to-volume ratio than their WT counterparts. The smaller mass-to-volume ratio is primarily due to the change in volume: when adjusted for body weight, the Marfan mice had significantly increased left ventricular volume, with little change in LV mass. Qualitative comparison of the normalized LV thickness also suggests that the Marfan mice may have slightly thicker walls than age-matched WT controls. The presence of dilated volumes with a near-normal wall thickness is suggestive of a dilated cardiomyopathy (DCM) phenotype, which is in agreement with previously reported findings on both humans and mouse models of MFS.^{27–29} However, it is not clear whether DCM is a primary finding, or secondary to abnormal hemodynamic loading conditions from other cardiovascular complications.^{27–34} One potential conflicting factor in our study was the impact of glycerol on tissue shrinkage. Glycerol has been shown to shrink tissue due to dehydration in a manner similar to air-immersion.³⁵ Moreover, as primary cardiomyopathy is still a debatable finding in MFS, we hypothesize that any glycerol-induced differences may be smaller than the pathophysiological differences.

To the best of our knowledge, this is the first demonstration of OCT for the cardiovascular phenotyping of adult mouse hearts. Unlike echocardiography, OCT is able to provide volumetric images of the heart at a much higher spatial resolution and is better able to visualize small structures such as fiber bundles and coronary vasculature. The high-resolution, 3-D nature of the acquired datasets allows researchers to better locate and study small changes in the heart morphology, since they provide both a global frame of reference, and a local, high-resolution visualization of the structures of interest, from which any number of planes can be virtually sectioned. Moreover, due to the nondestructive nature of OCT, specific areas identified in the dataset can be further isolated and studied using other complementary techniques, such as immunohistochemistry.

The analyses presented in this paper serve as a proof-of-concept for the use of OCT in quantifying changes in cardiac morphology. Using OCT, we were able to find significant differences in cardiac morphology between WT and Marfan mice. The morphological analyses can be further improved through the application of more sophisticated computational anatomy tools, including nonrigid registration, which would allow researchers to study subtle, localized changes in morphology, such as valve thickness and local wall thickness, in a non-destructive manner. We developed the methodology using fixed hearts as a sample, but this approach can also be extended to study cardiac contractile function by imaging *ex vivo* live hearts by performing gated OCT with faster light sources.^{36,37}

Acknowledgments

The authors would like to acknowledge funding support from the Canadian Institutes of Health Research (CIHR), Natural Sciences and Engineering Research Council of Canada (NSERC), and the Michael Smith Foundation for Health Research (MSFHR). G.F.T. is a Tier 1 Canada Research Chair.

References

1. V. Cañadas et al., "Marfan syndrome. Part 1: pathophysiology and diagnosis," *Nat. Rev. Cardiol.* **7**(5), 256–265 (2010).
2. D. P. Judge et al., "Evidence for a critical contribution of haploinsufficiency in the complex pathogenesis of Marfan syndrome," *J. Clin. Invest.* **114**(2), 172–181 (2004).
3. T. E. Bunton et al., "Phenotypic alteration of vascular smooth muscle cells precedes elastolysis in a mouse model of Marfan syndrome," *Circ. Res.* **88**(1), 37–43 (2001).
4. V. Marque et al., "Aortic wall mechanics and composition in a transgenic mouse model of marfan syndrome," *Arterioscler. Thromb. Vasc. Biol.* **21**(7), 1184–1189 (2001).
5. J. P. Habashi et al., "Losartan, an AT1 antagonist prevents aortic aneurysm in a mouse model of marfan syndrome," *Science* **312**(5770), 117–121 (2006).
6. M. Groenink et al., "Losartan reduces aortic dilatation rate in adults with Marfan syndrome: a randomized controlled trial," *Eur. Heart J.* **34**(45), 3491–500 (2013).
7. A. Madamanchi, "Mouse Models in Cardiology Research," *McGill J. Med.* **8**(5), 34–39 (2004).
8. M. L. Kirby and D. J. Sahn, "Mouse models of congenital heart defects: what's missing?," *Circ. Cardiovasc. Imaging* **3**(3), 228–230 (2010).
9. X. Liu et al., "Imaging techniques for visualizing and phenotyping congenital heart defects in murine models," *Birth Defects Res. C. Embryo Today* **99**(2), 93–105 (2013).
10. M. Scherrer-Crosbie and H. B. Thibault, "Echocardiography in translational research: of mice and men," *J. Am. Soc. Echocardiogr.* **21**(10), 1083–1092 (2008).
11. C. M. Ambrosi et al., "Virtual histology of the human heart using optical coherence tomography," *J. Biomed. Opt.* **14**(5), 054002 (2009).
12. W. J. Hucker et al., "Bimodal biophotonic imaging of the structure-function relationship in cardiac tissue," *J. Biomed. Opt.* **13**(5), 054012 (2008).
13. Y. Jian, K. Wong, and M. V. Sarunic, "Graphics processing unit accelerated optical coherence tomography processing at megahertz axial scan rate and high resolution video rate volumetric rendering," *J. Biomed. Opt.* **18**(2), 026002 (2013).
14. V. Westphal et al., "Correction of geometric and refractive image distortions in optical coherence tomography applying Fermat's principle," *Opt. Express* **10**(9), 397–404 (2002).
15. S. Ortiz et al., "Optical distortion correction in optical coherence tomography for quantitative ocular anterior segment by three-dimensional imaging," *Opt. Express* **18**(3), 2782–2796 (2010).
16. M. Zhao, A. N. Kuo, and J. A. Izatt, "3D refraction correction and extraction of clinical parameters from spectral domain optical coherence tomography of the cornea," *Opt. Express* **18**(9), 8923–8936 (2010).
17. L. Younes, *AMS 493. Lecture Notes, Topic: Mathematical Image Analysis*, John Hopkins University, Baltimore, Maryland (2008).
18. J. B. Keller and H. B. Keller, "Determination of reflected and transmitted fields by geometrical optics," *J. Opt. Soc. Am.* **40**(1), 48–52 (1950).
19. P. J. Burt and E. H. Adelson, "A multiresolution spline with application to image mosaics," *ACM Trans. Graph.* **2**(4), 217–236 (1983).
20. M. Brown and D. G. Lowe, "Automatic panoramic image stitching using invariant features," *Int. J. Comput. Vis.* **74**(1), 59–73 (2007).
21. J. C. Cauvin et al., "Automatic detection of the left ventricular myocardium long axis and center in thallium-201 single photon emission computed tomography," *Eur. J. Nucl. Med.* **19**(12), 1032–1037 (1992).
22. S. Dwivedi et al., "Automated cardiac pose computation from reconstructed myocardial SPECT images," *2011 IEEE Nucl. Sci. Symp. Conf. Rec.*, Valencia, Spain, pp. 2787–2794 (2011).

23. R. A. deKemp and C. Nahmias, "Automated determination of the left ventricular long axis in cardiac positron tomography," *Physiol. Meas.* **17**(2), 95–108 (1996).
24. D. E. Forman et al., "Cardiac morphology and function in senescent rats: gender-related differences," *J. Am. Coll. Cardiol.* **30**(7), 1872–1877 (1997).
25. M. W. Jenkins et al., "4D embryonic cardiography using gated optical coherence tomography," *Opt. Express* **14**(2), 736–748 (2006).
26. M. W. Jenkins et al., "Phenotyping transgenic embryonic murine hearts using optical coherence tomography," *Appl. Opt.* **46**(10), 1776–1781 (2007).
27. M. G. Keane and R. E. Pyeritz, "Medical management of Marfan syndrome," *Circulation* **117**(21), 2802–2813 (2008).
28. F. Alpendurada et al., "Evidence for Marfan cardiomyopathy," *Eur. J. Heart Fail.* **12**(10), 1085–1091 (2010).
29. J. R. Cook et al., "Abnormal muscle mechanosignaling triggers cardiomyopathy in mice with Marfan syndrome," *J. Clin. Invest.* **124**(3), 1329–1339 (2014).
30. L. J. Meijboom et al., "Evaluation of left ventricular dimensions and function in Marfan's syndrome without significant valvular regurgitation," *Am. J. Cardiol.* **95**(6), 795–797 (2005).
31. J. F. De Backer et al., "Primary impairment of left ventricular function in Marfan syndrome," *Int. J. Cardiol.* **112**(3), 353–358 (2006).
32. B. B. Das, A. L. Taylor, and A. T. Yetman, "Left ventricular diastolic dysfunction in children and young adults with Marfan syndrome," *Pediatr. Cardiol.* **27**(2), 256–258 (2006).
33. M. Rybczynski et al., "Tissue Doppler imaging identifies myocardial dysfunction in adults with marfan syndrome," *Clin. Cardiol.* **30**, 19–24 (2007).
34. A. Kiotsekoglou et al., "Early impairment of left ventricular long-axis systolic function demonstrated by reduced atrioventricular plane displacement in patients with Marfan syndrome," *Eur. J. Echocardiogr.* **9**(5), 605–613 (2008).
35. C. G. Rylander et al., "Dehydration mechanism of optical clearing in tissue," *J. Biomed. Opt.* **11**(4), 041117 (2006).
36. M. W. Jenkins et al., "In vivo gated 4D imaging of the embryonic heart using optical coherence tomography," *J. Biomed. Opt.* **12**(3), 030505 (2007).
37. W. Wieser et al., "Multi-megahertz OCT: high quality 3D imaging at 20 million A-scans and 4.5 G Voxels per second," *Opt. Express* **18**(14), 14685–14704 (2010).

Michelle Cua received her BSc degree in kinesiology, and her BAsC (Honors) and MASc degrees in biomedical engineering from Simon Fraser University (SFU). Her research is currently focused on the development of biomedical imaging technologies, including OCT, adaptive optics (AO), and microscopy, to better visualize and study the changes in retinal and cardiac morphology in response to pathological and environmental conditions.

Eric Lin received his PhD degree in physiology from University of British Columbia. He is investigating how hearts change their electrical properties to change their mechanical function, which allows them to function over a range of physiological conditions. Electrical and mechanical events in the heart are coupled by changes in intracellular calcium levels, and simultaneous voltage and calcium measurements are of interest, studied by combining traditional ECG and microelectrode techniques with modern optical mapping imaging techniques.

Ling Lee received her MSc degree in biomedical physiology and kinesiology (BPK) at SFU in 2014, and is currently a research assistant in Dr. Glen F. Tibbits' lab at the Child and Family Research Institute. Her graduate thesis involved evaluating the functional and structural cardiac properties of transgenic mouse models of Marfan syndrome *in vivo* using echocardiography.

Xiaoye Sheng received her MSc degree in kinesiology at SFU in 2005, and is working as a research technician for Dr. Glen F. Tibbits at the Child and Family Research Institute in Vancouver, BC. She is involved with echocardiography of Marfan mice, the study of ischemia reperfusion injury on neonatal hearts, and single cell calcium imaging.

Kevin S. K. Wong received a BAsC (Honors) degree in biomedical engineering at SFU in 2013, and is pursuing a master's degree with the Biomedical Optics Research Group at SFU. His graduate research concentrates on GPU computing for real-time OCT imaging and various applications of OCT, including speckle variance OCT, compressive sampling OCT, and wavefront sensorless adaptive optics OCT.

Glen F. Tibbits is a professor and chair in the Department of BPK at SFU, and a Tier 1 Canada Research Chair in Molecular Cardiac Physiology. His research interests focus on investigating the molecular and cellular mechanisms behind cardiac contractility and cardiac adaptation to various physiological, pathological, and environmental conditions.

Mirza Faisal Beg is a professor in the School of Engineering Science at SFU, and a Michael Smith Foundation for Health Research (MSFHR) Scholar. His research interests include signal and image processing, and the development of computational anatomy tools to study changes in anatomy (brain, retina, and heart) in response to diseases and treatments.

Marinko V. Sarunic is an associate professor in the School of Engineering Science at SFU and a MSFHR Scholar. His research interests in biomedical imaging include OCT, AO, and the use of GPUs for real-time processing and display.